ADVANCED MATERIALS
www.advmat.de

Microscopic Insights into Magnetic Warping and Time-Reversal Symmetry Breaking in Topological Surface States of Rare-Earth-Doped Bi_2Te_3

Beatriz Muñiz Cano, Fabián Calleja, Ji Dai, Massimo Tallarida, Vera Marinova, Alessandro Barla, Marc G. Cuxart, Pierluigi Gargiani, Gonzalo N. Molina, José Angel Silva-Guillén, Adriana I. Figueroa, Kevin García-Díez, Sergio O. Valenzuela, Aitor Mugarza, Amadeo L. Vázquez de Parga, Rodolfo Miranda, Francisco Guinea, Manuela Garnica, and Miguel A. Valbuena**

Magnetic interactions at the surface of topological insulators provide a versatile route to engineer exotic quantum states. Breaking time-reversal symmetry (TRS) at the topological surface state (TSS) enables the opening of a Dirac gap, which is essential for realizing quantum anomalous Hall physics. This work investigates the impact of submonolayer deposition of magnetic rare-earth adatoms on the prototypical topological insulator Bi_2Te_3. Scanning tunneling microscopy (STM) supported by first-principle calculations, core-level photoemission spectroscopy (XPS), angle-resolved photoemission spectroscopy (ARPES), X-ray magnetic circular dichroism (XMCD) and quasiparticle interference (QPI) mapping are combined to reveal direct evidence of local interactions between erbium (Er) atoms and the substrate, leading to significant modifications of the TSS. XMCD measurements confirm the out-of-plane magnetic anisotropy for Er adatoms on Bi_2Te_3, which induces a warping transition of the Fermi surface from a snowflake to a star-of-David-like geometry, along with a Dirac point gap opening and spectral splitting near the Γ point. QPI maps confirm the reconstructed surface band topology through modified scattering patterns consistent with TRS breaking. Our results identify a microscopic mechanism for magnetic interaction at the surface of a topological insulator and establish magnetic rare-earth doping as an effective strategy to tailor topological electronic states with atomic-scale control.

1. Introduction

Topological insulators (TIs) are quantum materials that exhibit an insulating bulk and conducting surface states protected by time-reversal symmetry (TRS). These topological surface states (TSSs) are characterized by a Dirac-cone-like dispersion and a helical spin texture, where the electron spin is locked perpendicular to its momentum. This spin-momentum locking arises from strong spin-orbit coupling (SOC) and confers robustness against non-magnetic disorder and backscattering, making TIs promising candidates for next-generation spintronic devices and quantum information technologies.[1,2] A central challenge, however, lies in controllably breaking TRS protection to engineer topologically nontrivial phases such as the quantum anomalous Hall effect (QAHE), which features dissipationless, spin-polarized edge currents in the absence of an external magnetic field.[3–5] One promising route is through the introduction of

---

B. M. Cano, F. Calleja, G. N. Molina, J. A. Silva-Guillén, A. L. V. de Parga, R. Miranda, F. Guinea, M. Garnica, M. A. Valbuena
Instituto Madrileño de Estudios Avanzados
IMDEA Nanociencia
Calle Faraday 9, Madrid 28049, Spain
E-mail: manuela.garnica@imdea.org; miguelangel.valbuena@imdea.org

The ORCID identification number(s) for the author(s) of this article can be found under https://doi.org/10.1002/adma.202510877

DOI: 10.1002/adma.202510877

J. Dai, M. Tallarida, P. Gargiani, K. García-Díez
ALBA Synchrotron Light Source
Cerdanyola del Vallès, Barcelona, Spain, 08290

V. Marinova
Institute of Optical Materials and Technologies
Bulgarian Academy of Sciences
Sofia 1113 Bulgaria

A. Barla
Istituto di Struttura della Materia (ISM)
Consiglio Nazionale delle Ricerche (CNR)
Trieste I-34149, Italy

M. G. Cuxart, K. García-Díez, S. O. Valenzuela, A. Mugarza
Catalan Institute of Nanoscience and Nanotechnology (ICN2), CSIC and BIST
Campus UAB
Barcelona 08193, Spain

magnetic order via proximity coupling or doping with magnetic impurities exhibiting out-of-plane magnetic anisotropy.[6–9] These perturbations can lift the Kramers degeneracy and open a bandgap at the Dirac point (DP).[10,11] However, achieving the QAHE remains experimentally challenging, as it often requires ultra-low temperatures, precise magnetic alignment, or complex material synthesis, such as in antiferromagnetic topological insulators (AFMTIs).[12–15] In this context, understanding and controlling the microscopic mechanisms that govern the interaction between magnetic moments and the spin texture of TSSs is crucial to unlocking the full potential of TIs in future electronic applications.

Recent observations of TRS breaking in the emerging class of AFMTIs have further intensified interest in magnetic interactions with TSSs, such as $MnBi_2Te_4$.[14] In these systems, an intrinsic antiferromagnetic coupling between out-of-plane aligned Mn layers within septuple-layered structures breaks TRS without the need for external doping, enabling the stoichiometric realization of magnetic topological phases. However, growth is challenging, leading to sample-dependent variations in their electronic structure and defect density, which can critically influence the presence or absence of magnetic ordering and the opening of a bandgap at the Dirac point.[16] These advances have stimulated theoretical efforts to understand the microscopic impact of magnetic perturbations on TSSs and to propose experimental spectroscopic fingerprints of TRS breaking. Notably, in TIs with strong SOC-induced warping,[17] theoretical models have recently predicted that the hexagonal symmetry of the Fermi surface (FS) is reduced to a trigonal one when a magnetic Zeeman term is introduced into the TSS Hamiltonian.[18–22] This symmetry-breaking effect should offer a direct spectroscopic signature of TRS violation, especially in cases where the detection of a bandgap is hindered by band broadening or overlap with bulk states. These predictions have recently been confirmed by angle-resolved photoemission spectroscopy (ARPES) measurements on Bi_2Se_2Te surfaces doped with magnetic rare-earth (RE) surface dopants such as erbium (Er) and dysprosium (Dy).[22]

RE doping has emerged as a highly effective strategy to induce long-range magnetic order in 2D quantum materials, due to the large spin and orbital magnetic moments of RE ions and their strong magnetic anisotropy,[23–31] which can ultimately maximize the magnetically induced bandgap at the DP[11] and potentially enable a robust QAHE at higher temperatures.[3] As an example, Dy doping on Bi_2Te_3 results in a large magnetic bandgap opening even at room temperature,[32,33] attributed to fluctuating, inhomogeneous magnetic patches with increasing size as the temperature decreases.[34] Furthermore, the surface deposition of one-third of a monolayer of Er (or Dy) on Bi_2Se_2Te at temperatures below their Curie points results in the lowering of the FS symmetry from warped hexagonal to trigonal[22] (a spectral fingerprint of TRS breaking) indicating the potential of RE surface dopants to interact with topological electronic states. Moreover, Er clusters or single atoms have been shown to exhibit hysteresis and out-of-plane magnetic anisotropy on close-packed metal surfaces.[24,25] Similarly, magnetic measurements and scanning tunneling spectroscopy (STS) experiments on Eu-doped Bi_2Te_3 have reported the appearance of a bandgap at the DP and indications of antiferromagnetic ordering at low temperatures.[35] In contrast, substitutional implantation of RE ions such as Gd, Ho, or Dy into the TI crystal lattice has not been found to induce magnetic order,[23] suggesting that the location and local environment of the magnetic dopants are critical. Remarkably, even isolated RE adatoms, such as Dy or Ho, on insulating substrates exhibit robust magnetic remanence and macroscopic spin relaxation times extending over hundreds or even thousands of seconds.[29,36] These findings highlight the unique capabilities of RE elements as surface dopants to stabilize magnetic moments and suggest a promising pathway for efficient interaction with TSSs under appropriate conditions.

In this work, we report on the surface doping of Er on the prototypical 3D TI substrate Bi_2Te_3, which hosts a strongly warped TSS. By combining a multidisciplinary set of experimental techniques, we investigate the interactions between surface magnetic dopants and the TSS at both microscopic and macroscopic levels. Locally, we identify the microscopic origin of the interactions through scanning tunneling microscopy and spectroscopy (STM/STS) and X-ray photoemission spectroscopy (XPS), supported by first-principles calculations. The effects of such interactions are reflected in the modifications observed in the TSS band dispersion, as revealed by ARPES. Remarkably, the characteristic "snowflake"-shaped warped FS of pristine Bi_2Te_3 is dramatically transformed into a "Star-of-David" FS pattern following the deposition of one-third of a monolayer of Er at very low temperature. This transformation can be interpreted as the superposition of two trigonal FS geometries with opposite orientations, consistent with the presence of magnetic impurities carrying out-of-plane moments of opposite sign as demonstrated by X-ray magnetic circular dichroism (XMCD). This scenario is further supported by local quasiparticle interference (QPI) patterns and is in

---

A. I. Figueroa
Departament de Física de la Matèria Condensada and IN2UB
Universitat de Barcelona
Barcelona 08028, Spain

S. O. Valenzuela, A. Mugarza
ICREA, Institució Catalana de Recerca i Estudis Avançats
Lluis Companys 23, Barcelona 08010, Spain

A. L. V. de Parga, R. Miranda
Departamento de Física de la Materia Condensada
Universidad Autónoma de Madrid (UAM)
Madrid 28049, Spain

A. L. V. de Parga, R. Miranda
Condensed Matter Physics Center (IFIMAC)
Universidad Autónoma de Madrid (UAM)
Madrid 28049, Spain

A. L. V. de Parga, R. Miranda, M. Garnica
Instituto Universitario de Ciencia de Materiales "Nicolás Cabrera"
Universidad Autónoma de Madrid
Madrid, Spain, 28049

F. Guinea
Donostia International Physics Center
Paseo Manuel de Lardizábal 4 San Sebastián 20018, Spain

F. Guinea
Ikerbasque
Basque Foundation for Science
Bilbao 48009, Spain

A. I. Figueroa
Institut de Nanociència i Nanotecnologia (IN2UB)
Universitat de Barcelona
Bilbao 08028, Spain

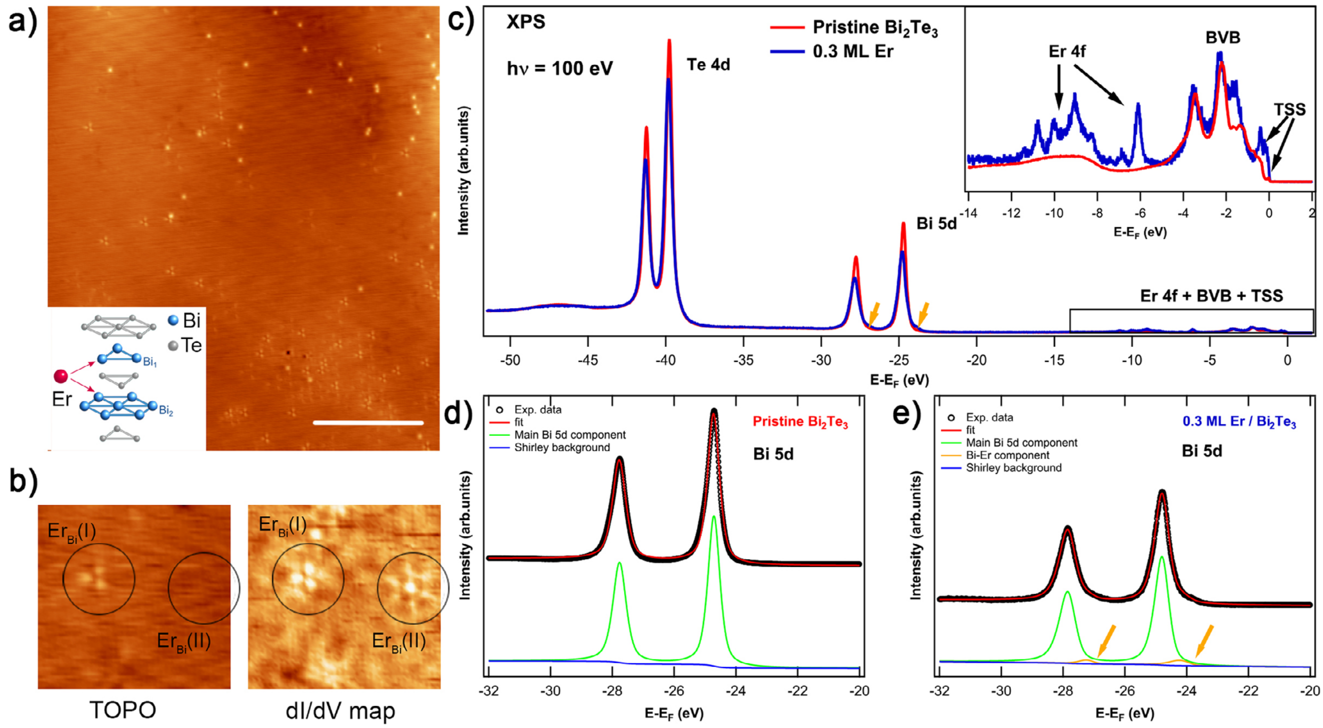

Figure 1. Structural characterization of Er on Bi_2Te_3. a) Topographic image of Bi_2Te_3 (V_b = 0.5 V and I_t = 1 nA, scale bar = 20 nm, T = 1.2 K) after Er deposition. Inset: Crystal structure of the Bi_2Te_3 (Bi = blue, Te = grey). After Er deposition, Er dopants (red) are incorporated into the Bi layers. b) Zoom-in and its corresponding dI/dV map at 0.5 V, where two point defects attributed to Er substitutions in the first and second Bi layers are observed. c) Comparison of the XPS overview spectra of pristine (red) and 0.3 ML Er doped Bi_2Te_3 (blue) showing Te 4d, Bi 5d core levels, Er 4f, bulk valence band (BVB), and topological surface state (TSS). The inset highlights the Er 4f, VB and TSS states indicated by the rectangle at the lower energy region at the XPS overview spectra. Multipeak fit of the XPS data of d) the pristine, and e) the 0.3 ML Er-doped samples. The intensity of the peaks decreases as Er is deposited, and a second component (orange peaks and arrows) emerges. Additionally, an energy shift is observed, consistent with a charge transfer between Er and the substrate. More details on the fitting procedure are provided in the Experimental Section.

agreement with theoretical predictions and previous experimental observations on related systems.[19,22]

Overall, these findings provide insight into the microscopic mechanisms behind magnetic interactions with TSSs and establish new strategies for tuning such interactions, opening viable pathways toward the realization of the QAHE. Our results offer unprecedented insight into the interplay between magnetism and topology and contribute to the development of next-generation quantum materials with engineered magnetic and topological functionalities.

2. Experimental Results

2.1. Surface and Chemical Characterization: Evidence of Local Er-Substrate Interactions

Bi_2Te_3 single crystals were grown by a modified Bridgman method in a standard crystal growth system. Exfoliation was performed in ultra-high vacuum (UHV), with the sample held at T = 15 K for XPS and ARPES measurements, and at room temperature (RT) for STM experiments. After cleaving, small amounts of Er were evaporated onto the freshly exposed surface. As shown in Figure S1 (Supporting Information), the Er atoms organize into well-defined islands on the surface. Additionally, high-resolution STM images reveal the appearance of multiple defects, see **Figure** 1a. While most of these defects correspond to previously reported and well-understood configurations,[37] two novel types of defect are observed, as highlighted in Figure 1b. In particular, one of these defects exhibits a distinctive flower-like shape in unoccupied-state dI/dV maps, most notably at 0.5 V (see Figure S2, Supporting Information). Since this feature has not been reported in pristine Bi_2Te_3, its presence is attributed to the Er deposition.

The XPS measurements were performed at the LOREA beamline of the ALBA synchrotron, acquired with $h\nu$ = 100 eV and at T = 15 K. Er coverage was estimated from the attenuation of the Bi $5d$ peaks. A detailed comparative analysis between pristine and 0.3 monolayer (ML) Er-doped Bi_2Te_3 is presented in Figure 1, while a similar analysis for a higher Er coverage of 1.2 ML is shown in Figure S5 (Supporting Information). The overview spectra in Figure 1c show highly intense and narrow peaks without any signs of extra components at higher binding energies (left side of the peaks), consistent with the absence of surface oxidation or contamination as well as very well-defined spin-orbit doublets. Additionally, no further disorder is introduced, as no broadening of the peak line shapes is detected after Er deposition. This is further evidenced by the very sharp and well-resolved multiplet structure of the highly localized Er $4f$ states at $E - E_F$ = 5–12 eV

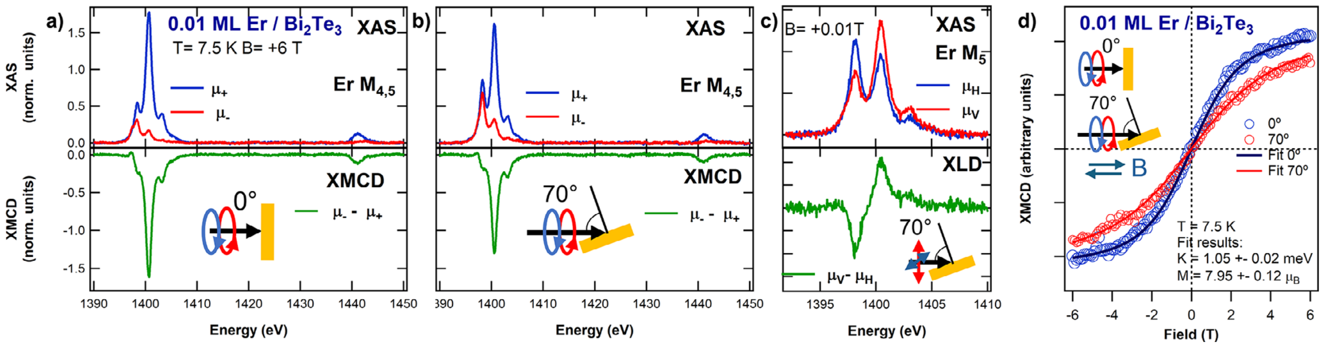

Figure 2. Magnetic characterization of 0.01 ML Er on Bi_2Te_3 by X-ray magnetic circular dichroism (XMCD) at T = 7.5 K. a) Normalized X-ray absorption spectra (XAS) with right- (μ_+, blue) and left-circularly (μ_-, red) polarized light at the Er $M_{4,5}$ edge (top), and the corresponding XMCD signal (μ_--μ_+, green, bottom), measured in total electron yield (TEY) mode under normal incidence (sensitive to out-of-plane magnetic moments) with an applied magnetic field B = +6 T, aligned with the X-ray beam and pointing along the surface normal. A schematic of the experimental geometry is shown. b) Same as in (a), but under grazing incidence (sensitive to in-plane magnetic moments). For direct comparison, XAS and XMCD spectra in both normal and grazing incidence are shown using the same intensity scale. c) Normalized XAS spectra with horizontal (μ_H, blue) and vertical (μ_V, red) linearly polarized light at the Er M_5 edge (top), and corresponding X-ray linear dichroism (XLD, μ_V-μ_H, green, bottom), measured in TEY mode at grazing incidence (sensitive to in-plane and out-of-plane charge anisotropy) and B = +0.01 T. d) Magnetization curves (open circles) extracted from the XMCD intensity at the main M_5 peak under normal (blue) and grazing (red) incidence. Solid lines are fits used to extract the total magnetic moment (M) and magnetic anisotropy energy per Er atom (K), as indicated in the insets (see Supporting Information for fitting details).

(magnified in the inset in Figure 1c). Importantly, the Bi_2Te_3 bulk valence band (BVB) and TSS are preserved after Er evaporation, as also indicated in the inset.

A closer inspection of the Bi 5*d* spectra (Figure 1d,e; Figure S5, Supporting Information) reveals several key features. First, an energy shift is observed (see Figure 1d; Figure S5, Supporting Information), consistent with charge transfer from Er to the substrate. Second, and more notably, a new spectral component appears in the Bi 5*d* core levels, as indicated by the orange peaks and arrows in Figure 1c,e. This component is likely associated with a direct interaction between Er surface dopants and Bi electronic states. This interpretation is further supported by the increasing intensity of this new component with higher Er coverage (Figure S5, Supporting Information). However, although the intensity of these Bi-related features increases with Er coverage, it does not scale proportionally with the total Er amount because part of the deposited Er forms islands observed in Figure S1 (Supporting Information), while only the fraction incorporated into the Bi layer contributes to this spectral component. A similar behavior has been reported in Er- and Dy-doped Bi_2Se_2Te, where an analogous feature in the Bi 5*d* peaks also increases with surface doping.[22] Consequently, this additional component ise attributed to a charge transfer effect resulting from the electronic interaction between Bi atoms and Er surface dopants.

2.2. Magnetic Anisotropy of Er Impurities Probed by XMCD

Breaking TRS in TIs can be induced by the interaction with magnetic impurities, particularly when their magnetic moments exhibit an out-of-plane component. To capture the intrinsic magnetic response of substitutional Er atoms, XMCD measurements were performed at very low coverages, consistent with the STM and XPS identification of Er atoms embedded in Bi sites, with special focus on magnetic anisotropy. The XMCD measurements were conducted at the BOREAS beamline of the ALBA synchrotron. Er atoms were deposited onto molecular beam epitaxy (MBE)-grown Bi_2Te_3 thin films, following a mild annealing process to remove the protective Te capping layer.[38] Since the pristine doping level of the MBE-grown Bi_2Te_3 films closely matches that of bulk crystals, the films can be regarded as representative of bulk-like samples.[39] Er was evaporated at a very low rate while the substrate was kept at base temperature (7.5 K). The coverage was estimated from the integrated average X-ray absorptionspectroscopy (XAS) signal. Two different coverages were investigated, corresponding approximately to 0.01 and 0.04 Er ML (**Figure 2** and Figure S10, Supporting Information, respectively). Under these growth conditions, the formation of mostly isolated atoms is expected,[25,40] although the presence of dimers or trimers[24] cannot be excluded.

Figure 2 summarizes the XAS, XMCD, and X-ray linear dichroism (XLD) characterization of the 0.01 ML Er system. A similar dataset is presented in Figure S10 (Supporting Information) for the 0.04 ML case. Panels (a) and (b) show the XAS and XMCD spectra measured at normal (0°) and grazing (70°) incidence, respectively. The peak structures of both coverages are characteristic of an Er^{3+} oxidation state.[25] A significantly stronger XMCD signal (approximately ~1/3 larger) is observed under normal incidence compared to grazing incidence, indicating that the easy axis of magnetization is out of plane. This confirms that the system exhibits pronounced out-of-plane magnetic anisotropy. For direct comparison, spectra in both geometries are plotted using the same intensity scale. This behavior closely resembles that of single Er atoms on close-packed heavy metal surfaces with strong SOC, such as Pt(111),[40] as well as Er atoms coordinated in metal-organic networks on Au(111).[30,41] In contrast, the opposite behavior is observed when Er is deposited on lighter substrates such as Cu(111), where the easy axis switches to in-plane.[25,40]

Panel (c) displays XAS and XLD spectra measured at grazing incidence using linearly polarized light. Horizontal polarization is mainly sensitive to in-plane charge anisotropy, while vertical

Table 1. Expectation values of the spin ($\langle S_z \rangle$), orbital ($\langle L_z \rangle$), and total ($\langle J_z \rangle = \langle S_z \rangle + \langle L_z \rangle$) magnetic moments, as well as the total magnetic moment ($M_T = 2\langle S_z \rangle + \langle L_z \rangle$), extracted from XMCD sum rules for normal (0°) and grazing (70°) incidence for Er atoms. The magnetic anisotropy energy per Er atom (K) and the total magnetic moment per atom (M) were obtained by fitting the magnetization curves.

0.01 Er ML	$\langle S_z \rangle$	$\langle L_z \rangle$	$\langle J_z \rangle$	M_T	K (meV)	M (μ_B)
0° (NI)	0.99(5)	4.12(5)	5.1(1)	6.1(1)	1.02 ± 0.02	7.95 ± 0.12
70° (GI)	0.65(5)	2.71(4)	3.4(1)	4.0(1)		

polarization probes the out-of-plane component. The resulting XLD signal (μ_V-μ_H) shows the characteristic line shape reported for other atomic or molecular Er systems with out-of-plane magnetic anisotropy: a negative peak at lower energies and an antisymmetric feature at higher energies.[30,41]

Expectation values of the orbital (L_z) and effective spin (S_{eff}) magnetic moments were extracted using XMCD sum rules.[42,43] The expectation values of the spin moment $\langle S_z \rangle$ in units of $\hbar$ were determined from the relation $\langle S_{\mathrm{eff}} \rangle = \langle S_z \rangle + 3\langle T_z \rangle$, assuming a constant ratio $\langle T_z \rangle / \langle S_z \rangle = +0.213$ for Er^{3+}.[41,44] This allows determining both $J_z = L_z + S_z$ and the total moment $M = L_z + 2S_z$. The resulting values are summarized in **Table 1**. The presence of a negative M_4 feature in the XMCD spectra is a clear fingerprint of strong orbital magnetism.

Panel (d) shows magnetization curves recorded by tracking the XMCD intensity at the main Er M_5 peak under ascending and descending magnetic fields, for both normal and grazing incidence. The most pronounced slope around fields close to 0 as well as the higher saturation magnetization in the normal configuration further support a strong out-of-plane magnetic anisotropy. To complement the sum-rule analysis, the magnetic anisotropy energy (MAE) per Er atom and its total magnetic moment can be obtained from the fitting of experimental magnetization curves measured at normal and grazing incidence.[45] Solid lines in Figure 2d correspond to the fitting results of the magneitzation curves. The obtained MAE (K) for the 0.01 Er ML is $K = 1.05 \pm 0.02$ meV / Er atom. The estimated MAE is similar, or even higher, than typical systems exhibiting strong out-of-plane magnetic anisotropy, as Co magnetic multilayers.[45,46]

Finally, the higher-coverage sample (4%) was also analyzed (see Figure S10 and Table S1, Supporting Information). Although the presence of dimers or small clusters leads to a reduction in the total moment per atom, the strong out-of-plane anisotropy is preserved, suggesting that it is an intrinsic feature of the Er/$\mathrm{Bi_2Te_3}$ system.

2.3. Electronic Properties

ARPES Measurements: Magnetically Induced Warping Transition of the TSS

ARPES measurements were performed using a photon energy of $h\nu = 52$ eV and at a temperature of $T = 15$ K at the LOREA beamline of the ALBA synchrotron, in order to characterize and evaluate the changes induced in the TSS FS and band dispersion following the deposition of 0.3 ML of Er on $\mathrm{Bi_2Te_3}$. The main results are summarized in **Figures 3**, **4**, S6 (Supporting Information), and 6. Figure 3 shows the FS, the electronic band dispersion of the TSS along the high-symmetry directions $\overline{\Gamma \mathrm{M}}$ and $\overline{\Gamma \mathrm{K}}$, and the corresponding momentum distribution curves (MDCs) along $\overline{\Gamma \mathrm{M}}$ for both the pristine (left) and Er-doped (right) samples. In Figure S6 (Supporting Information), second-derivative and curvature bandmaps along $\overline{\Gamma \mathrm{M}}$ are shown to better visualize the Er-modified TSS band dispersion.

The TSS of pristine $\mathrm{Bi_2Te_3}$ exhibits the typical FS pattern consistent with an hexagonal snowflake-like warping (Figure 3 left), and the circular-like shaped lower energy constant energy (CE) maps expected for rhombohedral 3D TIs (Figure 4 left). The warping strength arising from higher-order SOC terms is also consistent with the literature.[17,47] Consequently, the dispersion of the branches varies depending on the $\overline{\mathrm{K}\Gamma\mathrm{K}}$ or $\overline{\mathrm{M}\Gamma\mathrm{M}}$ directions. For instance, Figure 3b shows the cut along the $\overline{\mathrm{K}\Gamma\mathrm{K}}$ direction, corresponding to a cut perpendicular to the concave sides of the snowflake, resulting in an almost linear-like branch dispersion. In contrast, the bandmap in Figure 3c is obtained along the $\overline{\mathrm{M}\Gamma\mathrm{M}}$ direction, which coincides with the vertices of the snowflake, causing the branches of the TSS to bend near $\mathrm{E_F}$.[48] From the MDC stacking plot in Figure 3d, the position of the DP, defined by a single peak-like MDC, is determined to be 345 meV below $\mathrm{E_F}$, located within the bulk-projected bandgap in this case.

Transitioning to the Er-doped samples, the FS and TSS band dispersion in Figure 3 (right panel) reveal significant modifications compared to the pristine case. While the pristine sample exhibits the typical hexagonal snowflake-like warping, the Er-doped sample, strikingly, displays a faint star-of-David-like FS. As for the TSS bandmaps along the $\overline{\mathrm{K}\Gamma\mathrm{K}}$ direction (Figure 3f), no apparent modifications are observed apart from the expected broadening of the spectral features due to Er deposition, and a broadening in energy at the DP consistent with the opening of a Dirac gap, as discussed below. Nevertheless, along the $\overline{\mathrm{M}\Gamma\mathrm{M}}$ direction (Figure 3g), a subtle double shadow-like dispersion emerges. To analyze this effect in more detail, the MDC stacking plot in Figure 3h is examined. A splitting of the peaks corresponding to positive and negative k_x values with respect to the Γ high-symmetry point is observed. This is particularly evident in MDCs close to $\mathrm{E_F}$ (purple, dark blue, and pink curves): the left-side peak (negative k_x) evolves from a single peak in the pristine sample (Figure 3d) to a doublet in the doped sample (Figure 3h). A similar effect is also seen for the right-side peak (positive k_x), albeit more subtly—likely due to matrix element effects—which are also reflected in the reduced intensity on the positive k_x side of the FS in Figure 3e. This double-like dispersion is more clearly evidenced in second-derivative and curvature ARPES bandmaps along $\overline{\mathrm{M}\Gamma\mathrm{M}}$, as shown in Figure S6 (Supporting Information). Additionally, the red MDC corresponding to the DP allows for the extraction of its energy, located at 285 meV below $\mathrm{E_F}$, indicating the occurrence of p-type doping as a consequence of Er deposi-

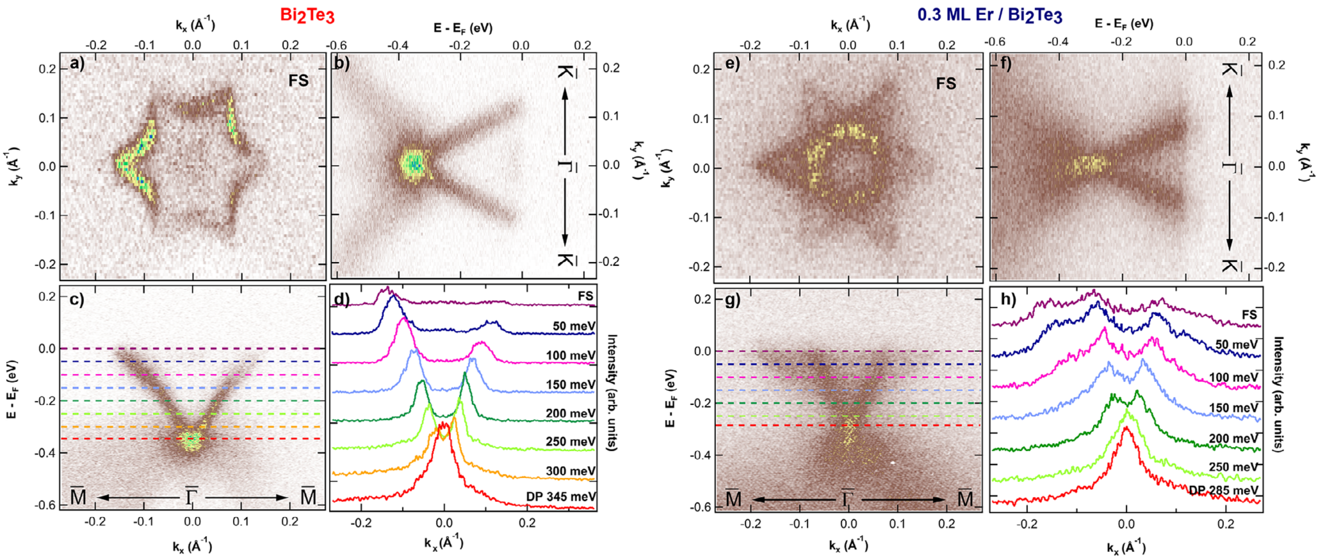

Figure 3. Angle-resolved photoemission spectroscopy (ARPES) characterization of pristine and Er-doped Bi_2Te_3. a–d) Data corresponding to the pristine Bi_2Te_3 surface. a) Fermi surface (FS) displaying the characteristic hexagonal snowflake-like warping of the topological surface state (TSS). b, c) TSS bandmaps along the $\overline{K\Gamma K}$ and $\overline{M\Gamma M}$ directions, respectively. While the dispersion in (b) is nearly linear—as the cut spans across the concave sides of the FS—the band in (c) shows a distinct curvature at the Fermi level (E_F), corresponding to the direction linking the FS vertices. d) Stacked momentum distribution curves (MDCs) extracted at selected energies in (c). e–h) Data for the 0.3 ML Er-doped Bi_2Te_3 surface. e) FS reveals a faint star-of-David-like warping of the TSS. f,g) Bandmaps along the $\overline{K\Gamma K}$ and $\overline{M\Gamma M}$ directions, respectively. The former shows a broadened spectrum compared to the pristine case, while the latter exhibits a marked double shadow-like dispersion absent in the undoped system. h) Stacked MDCs corresponding to the energies marked in (g), with color coding matching the horizontal dashed lines. The Dirac point (DP), highlighted in red, is located 285 meV below E_F, confirming *p*-type doping. A splitting of the MDC peaks around Γ is clearly observed for both positive and negative k_x values (notably in the purple, pink, and dark blue curves). All ARPES data were acquired with photon energy $h\nu = 52$ eV at $T = 15$ K.

tion. Similar *p*-type doping has also been observed in Er-doped Bi_2Se_2Te systems.[22]

Regarding the star-of-David FS and the double-peak band dispersion along $\overline{M\Gamma M}$, Figure 4 presents FS and CE maps, 2D curvature plots of the FS, and a schematic representation of the extracted contours from FS and CE maps for both the pristine (Figures 4a–f) and 0.3 ML Er-doped (Figure 4g–l) Bi_2Te_3 samples. The pristine hexagonal snowflake-like FS becomes more rounded as the binding energy increases in the CE maps. In contrast, the Er-doped Bi_2Te_3 sample clearly maintains a star-of-David-like pattern in the CE maps up to 100 meV. This observation is further supported by the double-peak dispersion extracted from MDC analysis, as well as from curvature and second-derivative TSS bandmaps along $\overline{M\Gamma M}$ shown in Figure S6 (Supporting Information). The 2D curvature plots (Figure 4b,h) provide improved clarity for discerning sharp features, despite challenges in fully eliminating background graining, which results in a somewhat smoothed appearance. From these plots, the FS contours can be extracted and are shown in purple in Figure 4f,l, along with additional contours extracted from the curvature-processed CE maps (not shown), following the energy-color correspondence with respect to Figure 3.

In the pristine sample, there is greater continuity in the snowflake shape compared to the star-of-David structure observed in the doped system, as seen more clearly in the extracted contours from the 2D curvature plots (Figure 4b,h). The latter appears to consist of two separate triangles with opposite orientations, rather than a single, continuous feature. This becomes particularly evident when analyzing the contours in Figures 4h and l, where the triangle sides are concave rather than straight, indicating a lack of continuity between the two triangular outlines, an observation that supports the proposed interpretation. This scenario is further supported by the idea that the double-like band structure of the TSS arises from two asymmetric TSS band dispersions, as indicated by the red and blue circles extracted from the MDC peak fitting analysis shown in Figure S6 (Supporting Information).

Finally, temperature-dependent measurements at $T = 35$ K, above the possible magnetic ordering temperature of Er, are shown in Figure S11. Comparison with the pristine sample reveals indications of both the gap and the star-of-David FS contour, suggesting that the gap may persist to much higher temperatures and could be attributed to fluctuating, inhomogeneous magnetic patches.[32–34]

QPI Signatures of TRS Breaking in Er/Bi_2Te_3: Local Interactions at the Atomic Scale

While ARPES provides a momentum-resolved but spatially averaged view of the occupied electronic structure, a local probe is essential to validate the proposed interpretation at the atomic scale. In this context, STS measurements enable access to electronic structure with atomic resolution, offering insight into spatial variations in the local density of states (LDOS) for occupied and unoccupied states.

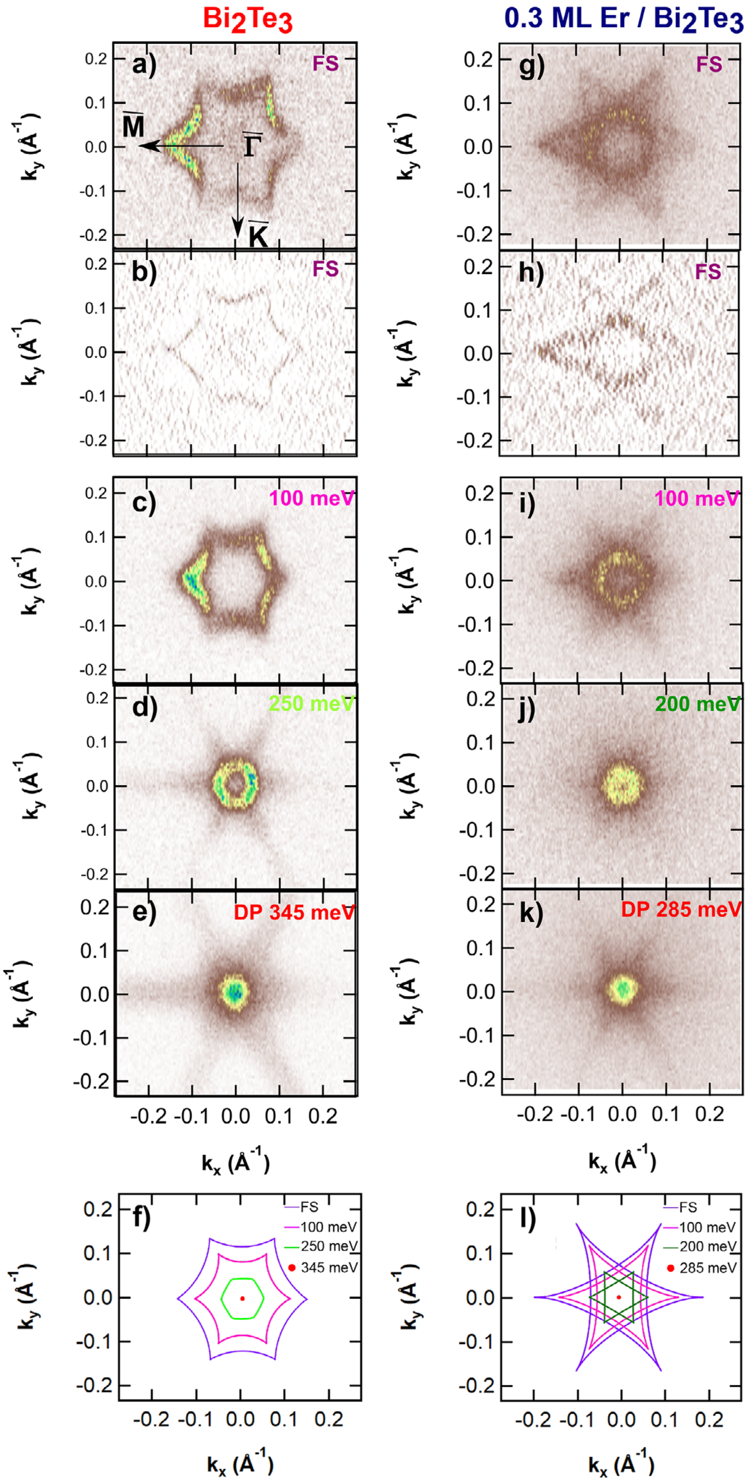

Figure 4. Experimental observation of the magnetically induced snowflake-to-star-of-David topological surface state (TSS) warping transition upon Er deposition, via angle-resolved photoemission spectroscopy (ARPES). **Left, pristine Bi$_2$Te$_3$** : a) Fermi surface (FS), b) 2D curvature-enhanced representations of the FS maps shown in (a) used to highlight the sharp features of the FS. c–e) Constant energy (CE) maps at 100, 250, and 345 meV (Dirac point, DP). The FS shows the characteristic snowflake-like hexagonal warping of the TSS, which progressively becomes more rounded as the energy moves away from E$_F$. f) Extracted FS and CE contours from panels (a, c–e). **Right, Er-doped Bi$_2$Te$_3$** : g) FS, (h) 2D curvature-enhanced representations of the FS maps shown in (g). i–k) CE maps at 100 meV, 200 meV, and 285 meV (DP). A star-of-David-like FS warping is clearly observed. Additionally, the DP is shifted toward E$_F$, indicating *p*-type doping. l) Extracted FS and CE contours from panels (a, c–e), revealing that the FS in the doped sample is composed of two distinct concave triangles rather than a deeper snowflake warping, thus indicating a qualitatively different warping mechanism. All ARPES data were acquired with photon energy $h\nu = 52$ eV at $T = 15$ K.

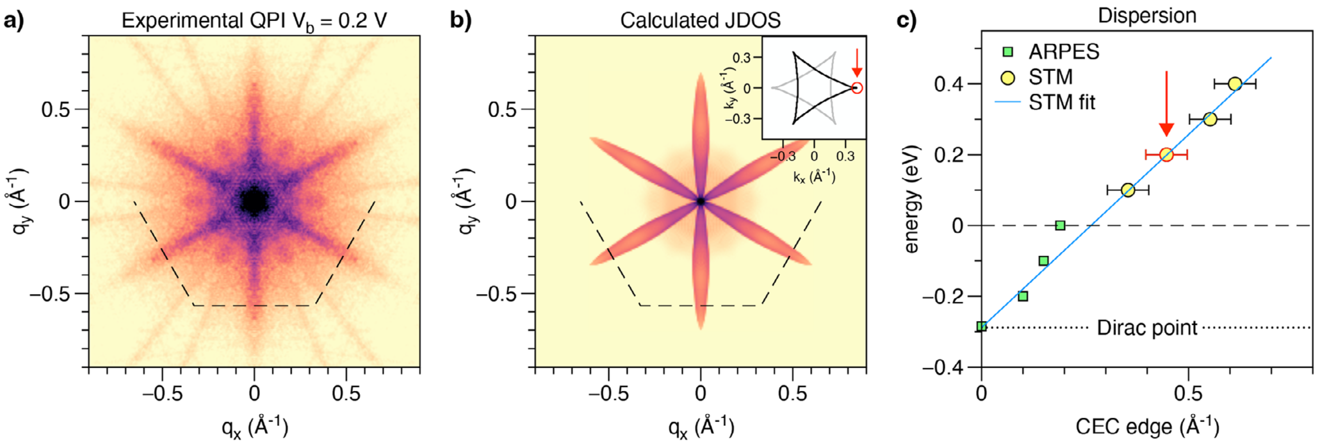

Figure 5. Experimental QPI map for Er-doped Bi_2Te_3 compared to joint density of states (JDOS) calculation and resulting energy dispersion. a) Symmetrized fast Fourier transformed (FFT) of a quasiparticle interference (QPI) map obtained on the surface of Er-deposited Bi_2Te_3 by means of STM at T = 1.2 K. The tip was stabilized at a bias voltage of 0.2 eV and a setpoint current of 1 nA. The dI/dV signal was obtained by means of a lock-in amplifier by adding a modulation of 50 mV and 763 Hz to the bias voltage. See main text and Supporting Information for more details. b) JDOS calculation resulting from the trigonal constant energy contour (CEC) shown in the inset. The JDOS was obtained as the self-convolution of the CEC including a back-scattering weight term, see main text for more details. Dashed black lines mark half of the SBZ, for reference. c) Dispersion relation obtained from the CECs employed to reproduce the experimental QPIs between 0.1 and 0.4 eV (yellow filled circles) and corresponding linear fit projected to estimate the Dirac point (blue line). The corresponding ARPES data for occupied states, extracted from Figure 3h, is represented as green filled squares.

As seen in the dI/dV map of Figure S2b (Supporting Information), surface electrons are scattered by the defects of the substrate, resulting in standing wave patterns in the LDOS. This process, known as Quasi-Particle Interference (QPI) is directly related to the electronic band structure of the system at the energy defined by the STM bias voltage. The experimental QPI maps recorded on Er-doped Bi_2Te_3 give rise to a very peculiar asterisk-like pattern along the $\overline{\Gamma M}$ directions, not reported for the case of pristine Bi_2Te_3 .[7,49] This pattern is shown in **Figure 5**a for the case of 0.2 V bias (unoccupied states), which is part of a bias series ranging from 0.1 to 0.4 V. In this series, a 80 nm side region was scanned at a resolution of 512 pixels, so that the atomic lattice spots fell inside the fast Fourier transformed (FFT) window (see Figure S7 in Supporting Information for the complete dataset). These were used as references for distortion correction and for determining the position of the SBZ (see dashed lines in Figure 5). The bias voltage was swept between 0.1 and 0.4 V while the current setpoint was held at 1 nA. In parallel, the dI/dV signal was recorded by means of a lock-in amplifier by adding a modulation of 50 mV at a frequency of 763 Hz to the bias voltage. The resulting dI/dV maps were FFT, distortion corrected and symmetrized following the crystal symmetry. The complete series, including the real space data as well as the raw and symmetrized FFT data, are presented in Figure S7 (Supporting Information).

In order to rationalize the peculiar QPI pattern obtained for Er-doped Bi_2Te_3 , we performed some basic joint density of states (JDOS) calculations, based on the two possible CEC geometries arising from the ARPES analysis: either trigonal, corresponding to the Er doped case, or hexagonal, corresponding to pristine Bi_2Te_3 . A detailed explanation of how we constructed these artificial CECs is given in the Supporting Information.

Then, for any given CEC, the corresponding JDOS was computed as the self convolution of the CEC weighted by a back-scattering factor, dependent on the relative orientation of the group velocity between the initial and final states, as commonly done in the literature.[7,50–53] An example of a particular CEC and its corresponding JDOS calculation is presented in Figure 5b, where the CEC is given as a black line in the inset. Here, we manually tuned all the CEC parameters in order to obtain a JDOS that matched the already mentioned asterisk-like pattern along the $\overline{\Gamma M}$ directions found in the experimental QPI of panel (a).

The first thing to note is that we could only reproduce reasonably well the experimental QPIs by using trigonal CECs, the hexagonal ones did not produce anything close to the asterisk-like pattern along the $\overline{\Gamma M}$ directions. This is illustrated in Figure S8 (Supporting Information), where an experimental QPI is compared to JDOS calculations based on trigonal and hexagonal CECs. This result, which is independent of the intensity of the CEC warping (as shown for both geometries in Figure S9, Supporting Information), supports the scenario proposed by the ARPES analysis discussed in the preceding sections and suggests that the trigonal CEC extends into the unoccupied states above the Fermi level.

Once the CEC parameters were established to match the experimental QPI at 0.2 V, as illustrated in Figure 5, we then proceeded to change only the overall CEC size (R parameter) in order to track the change in size of the experimental asterisk-like pattern at the different bias voltage values. The resulting JDOS patterns are presented in the lower row of Figure S7 (Supporting Information), together with the complete experimental dataset. Note that the R parameter corresponds exactly to the CEC edge, as illustrated by the red circle and arrow in the inset of Figure 5b. The resulting R values of the complete series are presented in panel (c) as yellow filled circles. A linear fit to them (blue line) yields a projection of the DP of the order of –0.3 eV, in agreement with the ARPES data presented in the previous sections (represented here as green filled squares).

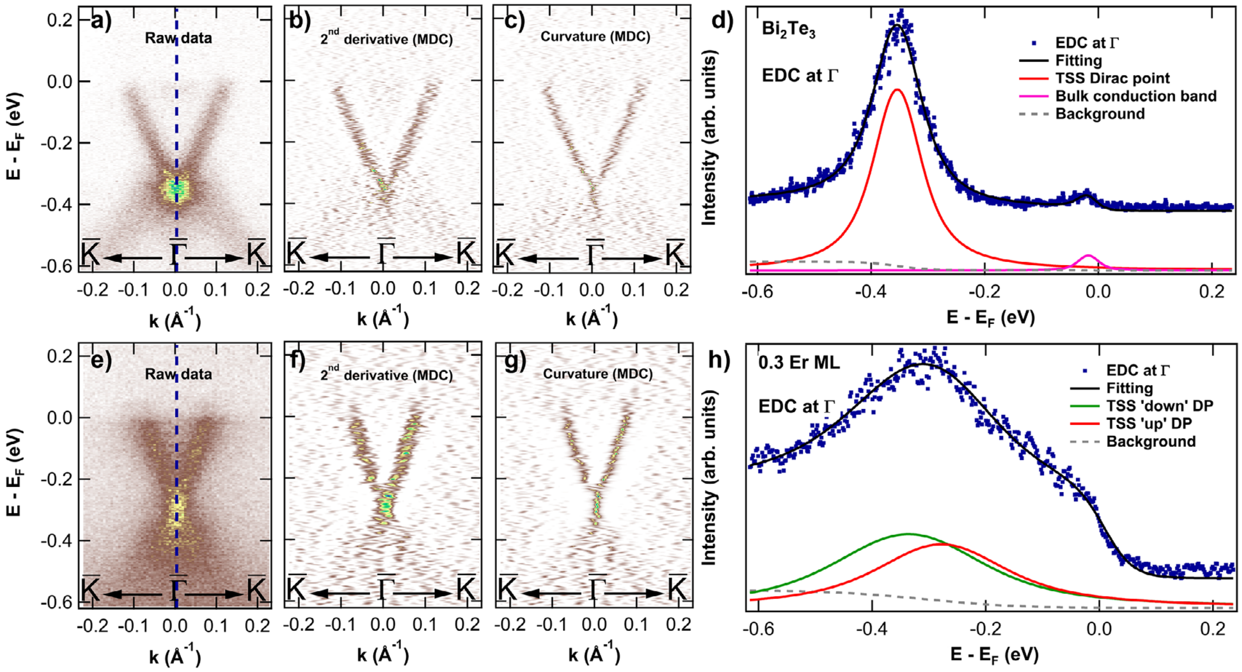

Figure 6. Evidence of Dirac point (DP) gap opening upon Er deposition in Bi_2Te_3 . a–d) Data for the pristine sample. a–c) ARPES bandmaps of the topological surface state (TSS): raw data (a), curvature-enhanced (b), and second derivative (c). (d) EDC at Γ showing a single sharp and intense peak, consistent with a well-defined, ungapped DP. e–h) Corresponding data for the 0.3 ML Er-doped sample. e–g) Raw, curvature, and second-derivative bandmaps, respectively, reveal a modification of the TSS near the DP. h) EDC at Γ displays a clear double-peak structure, corresponding to the upper and lower TSS branches, confirming the opening of a gap at the Dirac point induced by Er doping.More details on the fitting procedure are provided in the Experimental Section.

Therefore, QPI maps acquired on the Er-doped Bi_2Te_3 surface are compatible with a scattering pattern originating from a trigonal energy contour, which is consistent with the scenario of coexisting magnetic domains with opposite out-of-plane orientations. These real-space observations provide complementary and local support to the macroscopic ARPES results, reinforcing the interpretation of the star-of-David FS as a consequence of asymmetric, Zeeman-driven spin textures coexisting at the surface.

Bandgap Opening at the Dirac Point

These observations, i.e., the interpretation of the FS geometry as a signature of TRS breaking induced by magnetic impurities or domains with out-of-plane magnetic moments, prompt consideration of a possible bandgap opening, as theoretically expected under TRS breaking. **Figure 6** provides a detailed analysis of this effect. Figure 6a–c shows the raw, curvature-enhanced, and second-derivative MDC ARPES bandmaps of the TSS of the pristine Bi_2Te_3 sample acquired along the $\overline{K\Gamma K}$ direction. In contrast, Figure 6e–g displays the corresponding bandmaps for the 0.3 ML Er-doped Bi_2Te_3 sample. First, a clear *p*-type doping is evidenced by a shift of the DP out of the bulk band projection and closer to E_F . Second, the well-defined, localized DP observed in pristine Bi_2Te_3 evolves into a broadened, elongated intensity region around the DP in the doped case, as clearly seen by comparing the upper and lower panels in Figure 6.

A more conclusive analysis can be obtained from multipeak fitting of the energy distribution curves (EDCs) at Γ, which directly probes the presence of a bandgap. These EDCs are shown in Figure 6d,h for the pristine and doped samples, respectively. In the pristine sample, the EDC exhibits a sharp, narrow, and intense peak that can be fit with a single main peak corresponding to the DP (red), along with a smaller peak associated with the bulk conduction band (pink), closer to E_F . In contrast, the EDC of the 0.3 ML Er-doped sample is significantly broader due to the more diffuse spectral weight in the TSS band, necessitating an additional peak in the fit. In this case, the DP is no longer represented by a single narrow feature but instead appears as two broader peaks corresponding to the lower (green) and upper (red) components of the gapped TSS. This behavior is similar to the multipeak fits previously observed in Er-doped Bi_2Se_2Te ,[22] and it indicates a bandgap opening with an approximate width of 60 meV, consistent with the 70 meV gap reported for Bi_2Se_2Te . Furthermore, the multipeak analysis provides additional evidence of *p*-type doping induced by Er deposition. As a result, the pink peak corresponding to the bulk conduction band vanishes in the doped sample, suggesting a shift of the Fermi level and the possibility of the DP aligning with E_F .

3. Discussion

The deposition of Er onto the Bi_2Te_3 surface results in the formation of small islands and the emergence of a previously unobserved type of defect, as revealed by STM. These features are distinct in morphology and spatial distribution from intrinsic defects commonly seen in pristine Bi_2Te_3 .[37]

Based on their topographic signature and depth contrast in the STM images, we tentatively identify these defects as arising from Er atoms substituting Bi atoms within the Bi layers of the first quintuple layer. This hypothesis is further supported by the XPS data, which show the appearance of an additional component in the Bi 5d core-level spectrum. The intensity of this new spectral feature increases with Er coverage (see Figure 1; Figure S5, Supporting Information), suggesting a direct chemical interaction between Er and Bi atoms. Importantly, the intensity of this feature does not scale proportionally with the total amount of Er present on the surface, indicating the presence of two distinct Er-related contributions. On one hand, a fraction of the Er atoms interacts chemically with Bi, leading to the new spectral component in the Bi 5d region. This contribution correlates with the substitutional-type defects observed in STM and is attributed to Er atoms occupying Bi sites beneath the surface. On the other hand, the dominant contribution to the Er 4f signal originates from Er atoms that form islands on the surface, as clearly observed in the STM topographies. These islands do not induce noticeable changes in the Bi core levels, suggesting that the Er islands are more metallic-like or weakly bonded to the substrate.

In contrast, the Te core levels remain largely unaffected across all Er coverages, showing no discernible new features and only a very slight energy shift of ~80 meV, as observed in Figure S5 (Supporting Information). This is consistent with a small charge transfer from the Te layers toward Er, likely associated with the Er islands organized on the surface, and is also in line with the *p*-type doping observed in ARPES. This observation suggests that the chemical interaction upon Er deposition is more selective toward Bi atoms, while the Te sublattice remains largely unperturbed. The combination of STM and XPS data thus provides a consistent microscopic picture of local Er–Bi substitution and its structural and electronic fingerprints.

To further support our interpretation, we have performed STM simulations for Er atoms located in various atomic configurations (see Figures S3 and S4 from the Supporting Information). Specifically, we considered: (i) Er adatoms adsorbed at hollow and atop sites on the Bi_2Te_3 surface; (ii) Er substituting a Te atom in the topmost layer ($Er_{Te(1)}$); (iii) Er substituting Bi atoms in the first and second Bi layers of the first quintuple layer ($Er_{Bi(1)}$ and $Er_{Bi(2)}$, respectively); and (iv) a pair of adjacent Er adatoms. By directly comparing these simulated STM signatures with our experimental data (see Figure S3, Supporting Information), we assign the new type of defect shown in Figure 1 to an Er atom substituting a Bi atom in the second Bi layer ($Er_{Bi(2)}$). Furthermore, a distinct triangular-shaped defect observed in our STM measurements can be attributed to Er substitution in the first Bi layer ($Er_{Bi(1)}$). Notably, this triangular feature closely resembles defects previously reported as Te atoms substituting Bi sites[37] highlighting the need of careful interpretation of STM signatures. Our simulations thus provide strong microscopic validation for the assignment of the observed defects to specific Er configurations within the Bi_2Te_3 lattice.

Thus, regarding the electronic structure, the ARPES and STS results provide compelling evidence that surface doping of Bi_2Te_3 with Er induces significant modifications in the TSS. The transformation of the FS from a hexagonal shape to a star-of-David geometry indicates a strong distortion of the electronic states in momentum space. Furthermore, the emergence of an asymmetric double-peak dispersion in the TSS band along the $\overline{M\Gamma M}$ direction, along with the observation of a FFT compatible with a scattering pattern resulting from a triangular CEC, all suggest that TRS is broken at the surface. These signatures are further corroborated by the appearance of a finite energy gap at the DP, a hallmark of TRS breaking in topological insulators. Moreover, detailed analysis of EDCs reveals a shift in the chemical potential consistent with *p*-type doping in the Er-modified samples. Taken together, these spectroscopic findings—observed both in momentum-resolved (ARPES) and real-space (STM) measurements—highlight the impact of out-of-plane magnetic moments, likely associated with the Er 4f electrons, in altering the spin texture of the TSS. Consistently, XMCD measurements show that Er impurities deposited on Bi_2Te_3 exhibit clear out-of-plane magnetic anisotropy accompanied by large magnetic moments.

This interpretation agrees with previous theoretical[18–21] and experimental[22] studies that predict and confirm a transition of the FS shape from hexagonal to trigonal, along with asymmetric TSS band dispersion, upon the introduction of an out-of-plane Zeeman magnetic term in the Hamiltonian governing the warped hexagonal TSS.[17] In our case, the observation of a FS composed of two concave-sided triangular contours, together with the asymmetric double-like dispersion of the TSS, is compatible with a scenario in which the Er impurities may locally exhibit opposite out-of-plane magnetic orientations. Such a configuration would effectively result in two Zeeman terms of opposite sign, giving rise to two mirrored trigonal FS components. Given that ARPES is a spatially averaging technique, with a probing area on the order of tens of microns in this experiment, the spectral signature of the TSS reflects a superposition of eventual local magnetic domains with antiparallel out-of-plane moments, as expeccted in the absence of external magnetic field and the low temperature relative to the Er ordering temperature.[54] Similar observations have been proposed, for instance, for Eu-doped Bi_2Te_3 systems[35] and for fluctuating magnetic domains in Dy-doped Bi_2Te_3 materials.[33] This interpretation aligns with our experimental observations and offers a microscopic basis for the coexistence of multiple magnetic configurations contributing to the modified FS geometry.

4. Conclusion

In conclusion, this work provides direct evidence of the microscopic mechanisms underlying the spectral fingerprints of TRS breaking resulting from the interaction between magnetic RE (Er) surface dopants and the TSS of Bi_2Te_3. Through the appearance of a previously unreported atomic-scale defect observed by STM, the emergence of a distinct dI/dV signature absent in the pristine system, and the detection of a new spectral component in the Bi 5*d* XPS core levels, we identify the local electronic and structural perturbations induced by Er atoms. From these atomic-scale signatures of local interaction, we observe their macroscopic spectroscopic consequences: the transformation of the hexagonally warped FS into a star-of-David geometry, the emergence of asymmetric double-peak dispersion of the TSS, its counterpart in the form of QPI patterns at the local scale, and, importantly, the opening of a bandgap at the DP together with a *p*-type doping of the TSS, as well as the out-of-plane magnetic character of Er impurities revealed by XMCD. Together, these results establish a link between local magnetic perturbations and global modifications of the topological electronic structure, indicating TRS-breaking induced by locally oriented oppositely out-of-plane magnetic moments. Beyond fundamental insight, our findings offer a practical route for engineering magnetic topological phases, bringing us closer to the realization of exotic quantum phenomena such as the QAHE in engineered material platforms.

5. Experimental Section

Growing Methods: Bi_2Te_3 single crystals were grown by a modified Bridgman method in a standard crystal growth system and characterized by X-ray powder diffraction and Raman spectroscopy showing high crystal quality and crystalline long-range order with monocrystalline areas of typical dimensions of 5 x 3 x 0.1 mm^3. The crystals were mechanically exfoliated in situ at $T = 15$ K (base temperature) to minimize the induced density of defects prior to ARPES and XPS measurements, and at RT for STM measurements. RE were sublimated from an e-beam evaporator and deposited on a freshly cleaved Bi_2Te_3 surface at RT. Previously and in order to avoid oxide deposition, the RE were outgassed for more than 24 hours. The Er coverage of the samples was calculated using the Beer-Lambert law,[55,56] which describes the attenuation of radiation passing through a material, applied to XPS experiments. Bi_2Te_3 thin films for XAS and XMCD experiments were grown by molecular beam epitaxy (MBE) with a protective Te capping layer, which was subsequently removed by soft annealing and monitored by XAS measurements at the Te $M_{4,5}$ edge. More details can be found in Ref. [38].

XAS and XMCD Experiments: X-ray absorption spectroscopy (XAS), X-ray magnetic circular dichroism (XMCD), and X-ray linear dichroism (XLD) measurements were carried out at the BOREAS beamline of the ALBA synchrotron (Spain).[57] Experiments were conducted in total electron yield (TEY) mode using a 90% circularly polarized X-ray beam at a base temperature of 7.5 K. Circularly polarized absorption spectra were recorded at the Er $M_{4,5}$ edges under a magnetic field of 6 T, using both normal incidence (NI, 0°) and grazing incidence (GI, 70°) geometries. The XMCD signal was extracted as the difference between spectra with opposite helicities (XMCD $= \mu_- - \mu_+$) and normalized to the maximum intensity of the M_5 edge in the averaged spectrum. For the XLD measurements, absorption spectra at the Er M_5 edge were acquired with vertically and horizontally polarized linear light at 0.01 T in GI configuration. The XLD was calculated as XLD $= \mu_V - \mu_H$, where μ_V and μ_H correspond to the signals obtained with vertical and horizontal polarization, respectively. Spectra were normalized to the maximum of the isotropic M_5 edge.

Quantitative analysis of the XMCD spectra was performed using the sum rules,[42,43] assuming three holes for Er^{3+}. The orbital moment $\langle L_z \rangle$ and effective spin moment $\langle S_{eff} \rangle$ (in units of $\hbar$) were extracted, with the spin moment $\langle S_z \rangle$ derived from $\langle S_{eff} \rangle = \langle S_z \rangle + 3\langle T_z \rangle$. A constant ratio $\langle T_z \rangle / \langle S_z \rangle = +0.213$ was used for Er^{3+}.[44] The total angular momentum and total magnetic moment were then calculated as $\langle J_z \rangle = \langle L_z \rangle + \langle S_z \rangle$ and $M_T = \langle L_z \rangle + 2\langle S_z \rangle$, respectively.

ARPES and XPS Experiments: XPS and ARPES measurements were performed on the 3in situ exfoliated single crystals with a MBS hemispherical analyzer at the LOREA beamline[58,59] in ALBA Synchrotron, with linear horizontal light polarization and photon energies of $h\nu = 100$ and 52 eV, respectively.

A custom-made *Wavemetrics Igor Pro* routine was employed to fit the EDCs shown in Figure 6. The procedure accounts for the Fermi edge step and its temperature broadening, as well as for a Shirley-type background. The spectral peaks were fitted with Voigt functions, whose adjustable parameters include amplitude, width, energy position, and line-shape (continuously tunable from purely Gaussian to purely Lorentzian). For the pristine sample, the EDC at Γ is well described by a single peak associated with the TSS (red peak), together with a tiny contribution from bulk conduction band (purple peak). In contrast, for the 0.3 ML Er-doped sample, the EDC at Γ requires a double-peak fit, consistent with the opening of a band gap of approximately 60 meV between the lower branch of the TSS (red peaks) and the top of the bulk valence band (green peaks). Statistical uncertainties in the extracted peak positions are typically below ±10 meV, as estimated from the covariance matrix of the least-squares fit, ensuring that the observed gap is well above the fitting error.

The Bi 5*d* core-level spectra were analyzed using the *XPST* package implemented in *Wavemetrics Igor Pro*. The fits were performed with a multi-peak `MultiSK` line shape, combining Gaussian and Lorentzian components with an adjustable Gaussian-Lorentzian ratio (GL-ratio) and asymmetry parameters. Each spin-orbit component of the Bi $5d_{5/2}$-$5d_{3/2}$ doublet was modeled with a fixed energy separation of 3.06 eV and an intensity ratio $I_{5d_{3/2}}/I_{5d_{5/2}} \approx 0.75$, consistent across all spectra. The background was fitted simultaneously with the signal using a mixed polynomial-Shirley form including offset, linear term, and a pseudo-Tougaard contribution. The fitted parameters for each peak included area, binding energy position, full width at half maximum (FWHM), GL-ratio, and asymmetry, with typical statistical uncertainties below ±0.02 eV for the binding energies and ±0.01 eV for the FWHM. Relative errors in the integrated peak areas are in the range of 2–5 %, depending on the signal-to-noise ratio. These values, obtained from the covariance matrix of the fit, are significantly smaller than the spectral changes discussed in the manuscript, confirming that the additional Bi 5*d* component observed upon Er doping is statistically robust and not an artifact of the fitting procedure. Fits reports for Er-doped sample are shown in the supplementary information.

STM and QPI Maps Measurements: STM measurements were performed at 1.2 K on a custom-designed ultra high vacuum (UHV) system equipped with a Joule–Thompson scanning tunneling microscope. The crystal was cleaved by Scotch tape in situ at room temperature and directly transferred to the STM. The base pressure during the experiments was 2×10^{-10} mbar. STM topographic images were recorded in constant current mode. QPI maps were obtained by measuring the dI/dV signal by means of a lock-in amplifier by adding a modulation to the bias voltage, in constant current mode as well. The QPI maps were Fourier transformed, distortion corrected and symmetrized as described in the manuscript. All STM data analysis was done using the WSxM,[60] and the Image-Tank software.[61] The JDOS calculations were done by generating an array of the order of 800 points uniformly distributed over the selected CEC (either trigonal or hexagonal) and computing their self-convolution. The JDOS maps were obtained as the 2D histogram of the resulting q vectors, weighted as explained in the manuscript.

First-Principles Calculations: First-principles calculations were performed using density functional theory (DFT)[62,63] as implemented in SIESTA.[64–67] We used the generalized gradient approximation (GGA) and, in particular, the functional developed by Perdew et al.[68] Pseudopotentials were used to replace the core electrons.[69,70] We have used a split-valence double-ζ basis set including polarization functions.[64] The energy cutoff of the real space integration mesh was set to 400 Ry. The quintuple-layer structure of Bi_2Te_3 was optimized until the forces acting on the atoms were lower than 0.1 eV/Å using a uniform grid[71] of $(15 \times 15 \times 7)$ *k*-points. From that structure, we built a $7 \times 7 \times 3$ supercell of Bi_2Te_3. After including the different substitutions in the supercell, each structure was optimized the lattice vectors as well as the atomic positions with a threshold of 0.1 eV/Å and a $(1 \times 1 \times 1)$ *k*-grid. To simulate the STM images we use the Tersoff–Hamman approximation,[72] where the current is proportional to the local density of states at a specific tip position. For these calculations, we use a $(3 \times 3 \times 2)$ *k*-grid. We use WSxM to plot the STM data.[60]

Supporting Information

Supporting Information is available from the Wiley Online Library or from the author.

Acknowledgements

The authors acknowledge support by the Spanish Ministry of Science and Innovation and by the "European Union" (Grant no. PID2021-123776NB-C2, PID2021-128011NB-I00 and PID2024-157655NB-I00). IMDEA Nanociencia and IFIMAC acknowledge financial support from the Spanish Ministry of Science and Innovation "Severo Ochoa" (Grant CEX2020-001039-S) and "María de Maeztu" (Grant CEX2023-001316-M) Programme for Centres of Excellence in R&D, respectively. Financial support through the (MAD2D-CM)-MRR MATERIALES AVANZADOS-IMDEA-NC and (MAD2D-CM)-MRR MATERIALES AVANZADOS-UAM is acknowledged. This research received support from the Comunidad de Madrid through project TEC-2024/TEC-380 (Mag4TIC-CM). LOREA was cofunded by the European Regional Development Fund (ERDF) within the Framework of the Smart Growth Operative Programme 2014'2020. Authors thank Jordi Prat for the support during the beamtimes at LOREA. M.G. received financial support through the "Ramón y Cajal" Fellowship program (RYC2020-029317-I) and "Ayudas para Incentivar la Consolidación Investigadora" (CNS2022-135175). G.M., J.A.S.-G., and F.G. acknowledge financial support from NOVMOMAT, project PID2022-142162NB-I00 funded by MICIU/AEI/10.13039/501100011033 and by FEDER, UE. J.A. S-G. acknowledges financial support through the "Ramón y Cajal" Fellowship program, grant RYC2023-044383-I financed by MICIU/AEI/10.13039/501100011033 and FSE+. A.I.F. is a Serra Húnter fellow. G.M. acknowledges support from grant PREP2022-000457 funded by ICIU/AEI /10.13039/501100011033 and by FSE+. V.M. acknowledges the support by the Bulgarian Science Fund under the project number DFNI KΠ-06-H-68/1. S.O.V. acknowledges support from project PID2022-143162OB-I00 and Severo Ochoa Programme CEX2021-001214-S funded by MICIU/AEI/10.13039/501100011033 and by FEDER and from project TOCHA under Grant No. 824140 funded by EU's H2020 FET-PROACTIVE program. A. B. acknowledges financial support from project PRIN2022 "MAGNETISE" 2022KXN79M (Funded by the European Union - Next Generation EU, Mission 4 Component 1, CUP B53D23004280006). M.G.C. acknowledges funding from Severo Ochoa No. SEV-2013-0295. The authors sincerely thank Dr. Dhingra for his support and collaboration in the calibration of the Er. M.A.V. dedicates this work to the memory of his father, Antonio Valbuena.

Conflict of Interest

The authors declare no conflict of interest.

Data Availability Statement

The data that support the findings of this study are available from the corresponding author upon reasonable request.

Keywords

angle-resolved photoemission spectroscopy (ARPES), magnetic rare-earth doping, scanning tunneling microscopy (STM), time-reversal symmetry breaking, topological insulators

Received: June 9, 2025
Revised: October 22, 2025
Published online:

---

[1] M. Z. Hasan, C. L. Kane, *Rev. Mod. Phys.* **2010**, *82*, 3045.
[2] J. E. Moore, *Nature* **2010**, *464*, 194.
[3] J. Liu, T. Hesjedal, *Adv. Mater.* **2021**, *35*, 2102427.
[4] R. Yu, W. Zhang, H.-J. Zhang, S.-C. Zhang, X. Dai, Z. Fang, *Science* **2010**, *329*, 61.
[5] F. Fei, S. Zhang, M. Zhang, S. A. Shah, F. Song, X. Wang, B. Wang, *Adv. Mater.* **2020**, *32*, 1904593.
[6] S. Bhattacharyya, G. Akhgar, M. Gebert, J. Karel, M. T. Edmonds, M. S. Fuhrer, *Adv. Mater.* **2021**, *33*, 2007795.
[7] P. Sessi, P. Rüßmann, T. Bathon, A. Barla, K. Kokh, O. Tereshchenko, K. Fauth, S. Mahatha, M. Valbuena, S. Godey, F. Glott, A. Mugarza, P. Gargiani, M. Valvidares, N. H. Long, C. Carbone, P. Mavropoulos, S. Blügel, M. Bode, *Phys. Rev. B* **2016**, *94*, 075137.
[8] P. Rüßmann, S. K. Mahatha, P. Sessi, M. A. Valbuena, T. Bathon, K. Fauth, S. Godey, A. Mugarza, K. A. Kokh, O. E. Tereshchenko, P. Gargiani, M. Valvidares, E. Jiménez, N. B. Brookes, M. Bode, G. Bihlmayer, Stefan Blügel, P. Mavropoulos, C. Carbone, A. Barla, *J. Phys.: Mater.* **2018**, *1*, 015002.
[9] M. M. Otrokov, T. V. Menshchikova, I. Rusinov, M. Vergniory, V. M. Kuznetsov, E. V. Chulkov, *JETP Lett.* **2017**, *105*, 297.
[10] S.-Y. Xu, M. Neupane, C. Liu, D. Zhang, A. Richardella, L. Andrew Wray, N. Alidoust, M. Leandersson, T. Balasubramanian, J. Sánchez-Barriga, J. Sánchez-Barriga, O. Rader, G. Landolt, B. Slomski, J. H. Dil, J. Osterwalder, T.-R. Chang, H.-T. Jeng, H. Lin, A. Bansil, N. Samarth, M. Z. Hasan, *Nat. Phys.* **2012**, *8*, 616.
[11] Y. Chen, J.-H. Chu, J. Analytis, Z. Liu, K. Igarashi, H.-H. Kuo, X. Qi, S.-K. Mo, R. Moore, D. Lu, M. Hashimoto, T. Sasagawa, S. C. Zhang, I. R. Fisher, Z. Hussain, Z. X. Shen, *Science* **2010**, *329*, 659.
[12] C.-Z. Chang, J. Zhang, X. Feng, J. Shen, Z. Zhang, M. Guo, K. Li, Y. Ou, P. Wei, L.-L. Wang, Z.-Q. Ji, Y. Feng, S. Ji, X. Chen, J. Jia, X. Dai, Z. Fang, S.-C. Zhang, K. He, Y. Wang, L. Lu, X.-C. Ma, Q.-K. Xue, *Science* **2013**, *340*, 167.
[13] C.-Z. Chang, W. Zhao, D. Y. Kim, H. Zhang, B. A. Assaf, D. Heiman, S.-C. Zhang, C. Liu, M. H. Chan, J. S. Moodera, *Nat. Mater.* **2015**, *14*, 473.
[14] M. M. Otrokov, I. I. Klimovskikh, H. Bentmann, D. Estyunin, A. Zeugner, Z. S. Aliev, S. Gaß, A. Wolter, A. Koroleva, A. M. Shikin, M. Blanco-Rey, M. Hoffmann, I. P. Rusinov, A. Yu. Vyazovskaya, S. V. Eremeev, Yu. M. Koroteev, V. M. Kuznetsov, F. Freyse, J. Sánchez-Barriga, I. R. Amiraslanov, M. B. Babanly, N. T. Mamedov, N. A. Abdullayev, V. N. Zverev, A. Alfonsov, V. Kataev, B. Büchner, E. F. Schwier, S. Kumar, A. Kimura, et al., *Nature* **2019**, *576*, 416.
[15] E. D. Rienks, S. Wimmer, J. Sánchez-Barriga, O. Caha, P. S. Mandal, J. Růžička, A. Ney, H. Steiner, V. V. Volobuev, H. Groiß, M. Albu, G. Kothleitner, J. Michalicka, S. A. Khan, J. Minár, H. Ebert, G. Bauer, F. Freyse, A. Varykhalov, O. Rader, G. Springholz, *Nature* **2019**, *576*, 423.
[16] M. Garnica, M. M. Otrokov, P. C. Aguilar, I. Klimovskikh, D. Estyunin, Z. S. Aliev, I. R. Amiraslanov, N. A. Abdullayev, V. N. Zverev, M. B. Babanly, N. T. Mamedov, A. M. Shikin, A. Arnau, A. L. Vázquez de Parga, E. V. Chulkov, R. Miranda, *npj Quantum Mater.* **2022**, *7*, 1.
[17] L. Fu, *Phys. Rev. Letters* **2009**, *103*, 266801.
[18] Y. Imai, T. Yamaguchi, A. Yamakage, H. Kohno, *Phys. Rev. B* **2021**, *103*, 054402.
[19] G. Naselli, A. G. Moghaddam, S. Di Napoli, V. Vildosola, I. C. Fulga, J. van den Brink, J. I. Facio, *Phys. Rev. Research* **2022**, *4*, 033198.
[20] H. Tan, D. Kaplan, B. Yan, *Phys. Rev. Mater.* **2022**, *6*, 104204.
[21] D. Wang, H. Wang, D. Xing, H. Zhang, *arXiv:2205.08204*, **2022**.
[22] B. Muñiz Cano, Y. Ferreiros, P. A. Pantaleón, J. Dai, M. Tallarida, A. I. Figueroa, V. Marinova, K. García-Díez, A. Mugarza, S. O. Valenzuela, R. Miranda, J. Camarero, F. Guinea, J. A. Silva-Guillén, M. A. Valbuena, *Nano Lett.* **2023**, *23*, 6249.
[23] T. Hesjedal, *Phys. Status Solidi A* **2019**, *216*, 1800726.
[24] A. Singha, F. Donati, C. Wäckerlin, R. Baltic, J. Dreiser, M. Pivetta, S. Rusponi, H. Brune, *Nano Lett.* **2016**, *16*, 3475.

[25] A. Singha, R. Baltic, F. Donati, C. Wäckerlin, J. Dreiser, L. Persichetti, S. Stepanow, P. Gambardella, S. Rusponi, H. Brune, *Phys. Rev. B* **2017**, *96*, 224418.
[26] J. Jensen, A. R. Mackintosh, *Rare earth magnetism*, Clarendon Press Oxford, **1991**.
[27] M. Ormaza, L. Fernández, M. Ilyn, A. Magana, B. Xu, M. Verstraete, M. Gastaldo, M. Valbuena, P. Gargiani, A. Mugarza, A. Ayuela, L. Vitali, M. Blanco-Rey, F. Schiller, J. E. Ortega, *Nano Lett.* **2016**, *16*, 4230.
[28] L. Fernández, M. Blanco-Rey, R. Castrillo-Bodero, M. Ilyn, K. Ali, E. Turco, M. Corso, M. Ormaza, P. Gargiani, M. A. Valbuena, A. Mugarza, P. Moras, P. M. Sheverdyaeva, A. K. Kundu, M. Jugovac, C. Laubschat, J. E. Ortega, F. Schiller, *Nanoscale* **2020**, *12*, 22258.
[29] V. Bellini, S. Rusponi, J. Kolorenč, S. K. Mahatha, M. A. Valbuena, L. Persichetti, M. Pivetta, B. V. Sorokin, D. Merk, S. Reynaud, D. Sblendorio, S. Stepanow, C. Nistor, P. Gargiani, D. Betto, A. Mugarza, P. Gambardella, H. Brune, C. Carbone, A. Barla, *ACS nano* **2022**, *16*, 11182.
[30] S. O. Parreiras, D. Moreno, S. K. Mathialagan, B. Muñiz-Cano, C. Martín-Fuentes, M. Tenorio, L. Černa, J. I. Urgel, K. Lauwaet, M. Valvidares, M. A. Valbuena, J. M. Gallego, J. I. Martínez, P. Gargiani, R. Miranda, J. Camarero, D. Écija, *Nanoscale* **2023**, *15*, 7267.
[31] M. Blanco-Rey, R. Castrillo, K. Ali, P. Gargiani, M. Ilyn, M. Gastaldo, M. Paradinas, M. A. Valbuena, A. Mugarza, J. E. Ortega, F. Schiller, L. Fernández, *Small* **2024**, *20*, 2402328.
[32] S. Harrison, L. Collins-McIntyre, S. Zhang, A. Baker, A. Figueroa, A. Kellock, A. Pushp, S. Parkin, J. Harris, G. Van Der Laan, T. Hesjedal, *J. Phys.: Condens. Matter* **2015**, *27*, 245602.
[33] S. Harrison, L. J. Collins-McIntyre, P. Schönherr, A. Vailionis, V. Srot, P. A. van Aken, A. Kellock, A. Pushp, S. Parkin, J. Harris, B. Zhou, Y. L. Chen, T. Hesjedal, *Sci. Rep.* **2015**, *5*, 15767.
[34] L. B. Duffy, N.-J. Steinke, J. Krieger, A. I. Figueroa, K. Kummer, T. Lancaster, S. R. Giblin, F. L. Pratt, S. J. Blundell, T. Prokscha, A. Suter, S. Langridge, V. N. Strocov, Z. Salman, G. van der Laan, T. Hesjedal, *Phys. Rev. B* **2018**, *97*, 174427.
[35] S. Paul, M. Das, S. Datta, R. Chakraborty, P. Mandal, P. K. Giri, *J. Mater. Chem. C* **2024**, *12*, 15565.
[36] F. Donati, S. Rusponi, S. Stepanow, C. Wäckerlin, A. Singha, L. Persichetti, R. Baltic, K. Diller, F. Patthey, E. Fernandes, J. Dreiser, Ž. Šljivancanin, K. Kummer, C. Nistor, P. Gambardella, H. Brune, *Science* **2016**, *352*, 318.
[37] A.-M. Netsou, D. A. Muzychenko, H. Dausy, T. Chen, F. Song, K. Schouteden, M. J. Van Bael, C. Van Haesendonck, *ACS nano* **2020**, *14*, 13172.
[38] M. G. Cuxart, M. A. Valbuena, R. Robles, C. Moreno, F. Bonell, G. Sauthier, I. Imaz, H. Xu, C. Nistor, A. Barla, P. Gargiani, M. Valvidares, D. Maspoch, P. Gambardella, S. O. Valenzuela, A. Mugarza, *ACS Nano* **2020**, *14*, 6285.
[39] M. G. Cuxart, *Magnetic metal-organic/topological insulator heterostructures*, Universitat Autònoma de Barcelona, **2020**.
[40] F. Donati, A. Singha, S. Stepanow, C. Wäckerlin, J. Dreiser, P. Gambardella, S. Rusponi, H. Brune, *Phys. Rev. Letters* **2014**, *113*, 1.
[41] D. Moreno, S. O. Parreiras, J. I. Urgel, B. Muñiz-Cano, C. Martín-Fuentes, K. Lauwaet, M. Valvidares, M. A. Valbuena, J. M. Gallego, J. I. Martínez, P. Gargiani, J. Camarero, R. Miranda, D. Écija, *Small* **2022**, *18*, 2107073.
[42] B. Thole, P. Carra, F. Sette, G. van der Laan, *Phys. Rev. letters* **1992**, *68*, 1943.
[43] P. Carra, B. Thole, M. Altarelli, X. Wang, *Phys. Rev. Letters* **1993**, *70*, 694.
[44] P. Giannozzi, S. Baroni, N. Bonini, M. Calandra, R. Car, C. Cavazzoni, D. Ceresoli, G. L Chiarotti, M. Cococcioni, I. Dabo, A. D. Corso, S. de Gironcoli, S. Fabris, G. Fratesi, R. Gebauer, U. Gerstmann, C. Gougoussis, A. Kokalj, M. Lazzeri, L. Martin-Samos, N. Marzari, F. Mauri, R. Mazzarello, S. Paolini, A. Pasquarello, L. Paulatto, C. Sbraccia, S. Scandolo, G. Sclauzero, A. P. Seitsonen, et al., *J. Phys.: Condens. Matter* **2009**, *21*, 395502.
[45] P. Gambardella, S. Rusponi, M. Veronese, S. Dhesi, C. Grazioli, A. Dallmeyer, I. Cabria, R. Zeller, P. Dederichs, K. Kern, C. Carbone, H. Brune, *Science* **2003**, *300*, 1130.
[46] O. Šipr, S. Bornemann, H. Ebert, J. Minár, *J. Phys. Condens. Matter.* **2014**, *26*, 196002.
[47] Y. Chen, J. G. Analytis, J.-H. Chu, Z. Liu, S.-K. Mo, X.-L. Qi, H. Zhang, D. Lu, X. Dai, Z. Fang, S. C. Zhang, I. R. Fisher, Z. Hussain, Z.-X. Shen, *Science* **2009**, *325*, 178.
[48] J. Sánchez-Barriga, M. R. Scholz, E. Golias, E. Rienks, D. Marchenko, A. Varykhalov, L. V. Yashina, O. Rader, *Phys. Rev. B* **2014**, *90*, 195413.
[49] W. C. Lee, C. Wu, D. P. Arovas, S. C. Zhang, *Phys. Rev. B* **2009**, *80*, 245439.
[50] L. M. Roth, H. J. Zeiger, T. A. Kaplan, *Phys. Rev.* **1966**, *149*, 519.
[51] Q. Liu, X.-L. Qi, S.-C. Zhang, *Phys. Rev. B* **2012**, *85*, 125314.
[52] P. Leicht, J. Tesch, S. Bouvron, F. Blumenschein, P. Erler, L. Gragnaniello, M. Fonin, *Phys. Rev. B* **2014**, *90*, 241406.
[53] P. Rüssmann, P. Mavropoulos, S. Blügel, *Phys. Status Solidi (b)* **2021**, *258*, 2000031.
[54] J. Banister, S. Legvold, F. Spedding, *Phys. Rev.* **1954**, *94*, 1140.
[55] A. Beer, *Ann. Phys.* **1852**, *162*, 78.
[56] J.-H. Lambert, *Photometria, sive de Mensura et gradibus luminis, colorum et umbrae*, sumptibus viduae E. Klett, 1760.
[57] A. Barla, J. Nicolás, D. Cocco, S. M. Valvidares, J. Herrero-Martín, P. Gargiani, J. Moldes, C. Ruget, E. Pellegrin, S. Ferrer, *Synchrotron Radiat.* **2016**, *23*, 1507.
[58] G. García, M. Martin, M. Ynsa, V. Torres-Costa, M. Crespillo, M. Tardío, J. Olivares, F. Bosia, O. Peña-Rodríguez, J. Nicolas, M. Tallarida, *Eur. Phys. J. Plus* **2022**, *137*, 1157.
[59] A. Crisol, F. Bisti, C. Colldelram, M. Llonch, B. Molas, R. Monge, J. Nicolás, L. Nikitina, M. Quispe, L. Ribó, M. Tallarida, in *Proc. MEDSI'20*, Mechanical Engineering Design of Synchrotron Radiat. Equipment and Instrumentation, JACoW Publishing, Geneva, Switzerland, **2021**, pp. 14–16.
[60] I. Horcas, R. Fernández, J. M. Gómez-Rodríguez, J. Colchero, J. Gómez-Herrero, A. M. Baro, *Rev. Sci. Instrum.* **2007**, *78*, 013705.
[61] ImageTank, Imagetank website, https://visualdatatools.com/ImageTank/, **2024** (accessed: May 2025).
[62] P. Hohenberg, W. Kohn, *Phys. Rev.* **1964**, *136*, B864.
[63] W. Kohn, L. J. Sham, *Phys. Rev.* **1965**, *140*, A1133.
[64] E. Artacho, D. Sánchez-Portal, P. Ordejón, A. García, J. M. Soler, *Phys. Stat. Solidi (b)* **1999**, *215*, 809.
[65] J. M. Soler, E. Artacho, J. D. Gale, A. García, J. Junquera, P. Ordejón, D. Sánchez-Portal, *J. Phys.: Condens. Matter* **2002**, *14*, 2745.
[66] E. Artacho, E. Anglada, O. Diéguez, J. D. Gale, A. García, J. Junquera, R. M. Martin, P. Ordejón, J. M. Pruneda, D. Sánchez-Portal, J. M. Soler, *J. Phys.: Condens. Matter* **2008**, *20*, 064208.
[67] A. García, N. Papior, A. Akhtar, E. Artacho, V. Blum, E. Bosoni, P. Brandimarte, M. Brandbyge, J. I. Cerdá, F. Corsetti, R. Cuadrado, V. Dikan, J. Ferrer, J. Gale, P. García-Fernández, V. M. García-Suárez, S. García, G. Huhs, S. Illera, R. Korytár, P. Koval, I. Lebedeva, L. Lin, P. López-Tarifa, S. G. Mayo, S. Mohr, P. Ordejón, A. Postnikov, Y. Pouillon, M. Pruneda, et al., *J. Chem. Phys.* **2020**, *152*, 204108.
[68] J. P. Perdew, A. Ruzsinszky, G. I. Csonka, O. A. Vydrov, G. E. Scuseria, L. A. Constantin, X. Zhou, K. Burke, *Phys. Rev. Lett.* **2008**, *100*, 136406.
[69] M. van Setten, M. Giantomassi, E. Bousquet, M. Verstraete, D. Hamann, X. Gonze, G.-M. Rignanese, *Comput. Phys. Commun.* **2018**, *226*, 39.
[70] A. García, M. J. Verstraete, Y. Pouillon, J. Junquera, *Comput. Phys. Commun.* **2018**, *227*, 51.
[71] H. J. Monkhorst, J. D. Pack, *Phys. Rev. B* **1976**, *13*, 5188.
[72] J. Tersoff, D. R. Hamann, *Phys. Rev. B* **1985**, *31*, 805.